JGR Space Physics

RESEARCH ARTICLE
10.1029/2019JA027270

Impacts of Binning Methods on High-Latitude Electrodynamic Forcing: Static Versus Boundary-Oriented Binning Methods

Qingyu Zhu[1], Yue Deng[1], Arthur Richmond[2], Astrid Maute[2], Yun-Ju Chen[3], Marc Hairston[3], Liam Kilcommons[4], Delores Knipp[2,4], Robert Redmon[5], and Elizabeth Mitchell[6]

[1]Department of Physics, University of Texas at Arlington, Arlington, TX, USA, [2]High Altitude Observatory, National Center for Atmosphere Research, Boulder, CO, USA, [3]William B. Hanson Center for Space Sciences, University of Texas at Dallas, Richardson, TX, USA, [4]Aerospace Engineering Sciences, University of Colorado Boulder, Boulder, CO, USA, [5]National Center for Environmental Information (NCEI), National Oceanic and Atmospheric Administration (NOAA), Boulder, CO, USA, [6]The Johns Hopkins University Applied Physics Laboratory, Laurel, MD, USA

Key Points:
- High-latitude electron precipitation and electric potential data are binned through static and boundary-oriented binning approaches
- As compared with the static binning results, the boundary-oriented binning method provides a more confined and intense electron precipitation pattern and a potential pattern with higher cross polar cap potential
- Hemispherical-integrated Joule heating can vary by ~18% when different binning results are utilized to drive GCMs for the conditions studied

Correspondence to:
Y. Deng,
yuedeng@uta.edu

Citation:
Zhu, Q., Deng, Y., Richmond, A., Maute, A., Chen, Y.-J., Hairston, M., et al. (2020). Impacts of binning methods on high-latitude electrodynamic forcing: Static versus boundary-oriented binning methods. *Journal of Geophysical Research: Space Physics*, *125*, e2019JA027270. https://doi.org/10.1029/2019JA027270

Received 8 AUG 2019
Accepted 28 DEC 2019
Accepted article online 3 JAN 2020

Abstract An outstanding issue in the general circulation model simulations for Earth's upper atmosphere is the inaccurate estimation of Joule heating, which could be associated with the inaccuracy of empirical models for high-latitude electrodynamic forcing. The binning methods used to develop those empirical models may contribute to the inaccuracy. Traditionally, data are binned through a static binning approach by using fixed geomagnetic coordinates, in which the dynamic nature of the forcing is not considered and therefore the forcing patterns may be significantly smeared. To avoid the smoothing issue, data can be binned according to some physically important boundaries in the high-latitude forcing, that is, through a boundary-oriented binning approach. In this study, we have investigated the sensitivity of high-latitude forcing patterns to the binning methods by applying both static and boundary-oriented binning approaches to the electron precipitation and electric potential data from the Defense Meteorological Satellite Program satellites. For this initial study, we have focused on the moderately strong and dominantly southward interplanetary magnetic field conditions. As compared with the static binning results, the boundary-oriented binning approach can provide a more confined and intense electron precipitation pattern. In addition, the magnitudes of the electric potential and electric field in the boundary-oriented binning results increase near the convection reversal boundary, leading to a ~11% enhancement of the cross polar cap potential. The forcing patterns obtained from both binning approaches are used to drive the Global Ionosphere and Thermosphere Model to assess the impacts on Joule heating by using different binning patterns. It is found that the hemispheric-integrated Joule heating in the simulation driven by the boundary-oriented binning patterns is 18% higher than that driven by the static binning patterns.

1. Introduction

At Earth's high latitudes, the magnetosphere is closely coupled to the ionosphere and thermosphere (I-T) system. From a perspective of the energy exchange, most of the electromagnetic energy from the magnetosphere is deposited into the I-T system as Joule heating (Lu et al., 1995; Thayer et al., 1995), which has significant impact on the I-T system, especially during geomagnetic storms (e.g., Fuller-Rowell et al., 1994; Prölss, 1995). For example, Joule heating can effectively increase the neutral temperature, which induces the expansion and upwelling of the thermosphere, leading to an enhancement of the neutral density at higher altitudes. Joule heating can also modify the global circulation and excite gravity waves, and both of them can effectively broaden the impact of electromagnetic energy inputs on the I-T system to the whole globe. Therefore, an accurate estimation of Joule heating in general circulation models (GCMs) is crucial to improve the GCM simulations of the I-T system (Pedatella et al., 2018).

According to Lu et al. (1995), the Joule heating deposition rate (Q_J) can be expressed as follows:

$$Q_J = \sigma_p(\mathbf{E} + \mathbf{U_n}\times\mathbf{B_0})^2 \quad (1)$$

Here σ_p is the Pedersen conductivity, which is influenced by the solar irradiation and the particle precipitation, and with the latter dominant on the night side (Wallis & Budzinski, 1981). $\mathbf{E}$ and $\mathbf{U_n}$ are the ionospheric electric field and neutral wind in the Earth's reference frame, respectively, and $\mathbf{B_0}$ represents the geomagnetic main field. Specifications of the ionospheric electric field and particle precipitation are critical for Joule heating estimation, because they not only explicitly contribute to Joule heating by changing $\mathbf{E}$ and σ_p but also strongly influence the neutral winds ($\mathbf{U_n}$) through the ion-drag force (Killeen & Roble, 1984). Therefore, their specifications are the main focus of this study.

In spite of the dynamic nature of the high-latitude electric field and particle precipitation, great efforts have been made to advance our understanding of their morphologies under different conditions during the past several decades, and their large-scale pictures have been well established:

1. For the particle precipitation, it is known that intense particle precipitations mainly occur within a ring-shaped region encompassing the geomagnetic pole, namely, the auroral oval, which can be identified from both in-situ particle observations (e.g., Newell et al., 1991, 1996; Redmon et al., 2010; Kilcommons et al., 2017) and auroral emission observations (e.g., Baker et al., 2000; Ding et al., 2017; Holzworth & Meng, 1975). The shape and the location of the auroral oval and the intensity of the particle precipitation change with the geomagnetic activity, season, and solar activity (e.g., Hardy et al., 1987; Liou et al., 2001; Luan et al., 2018). Moreover, the more dynamic evolutions of the particle precipitations are frequently found during substorms (e.g., Akasofu, 1964; Liou et al., 2006).
2. The ionospheric electric field is associated with the ion drifts in the ionosphere, which depends on the interplanetary magnetic field (IMF) conditions, seasons, etc. It is found that the ion convection displays a two-cell pattern when the IMF is southward (Dungey, 1961). The relative sizes of the convection cells on the dawnside and duskside are also dependent on the dawn-dusk component of the IMF (Burch et al., 1985; Reiff & Burch, 1985). Ions drift antisunward at higher latitudes and sunward at lower latitudes. The location separating sunward and antisunward ion drifts is referred to as the convection reversal boundary (CRB), which is well aligned with the open-closed field line boundary (OCB) especially when B_z is southward (e.g., Drake et al., 2009; Sotirelis et al., 2005). Variations of the CRB under different conditions have been extensively investigated in previous studies (e.g., Bristow & Spaleta, 2013; Chen et al., 2015; Chen & Heelis, 2018; de la Beaujardiere et al., 1991; Hairston & Heelis, 1990; Koustov & Fiori, 2016).

Based on the climatological studies of high-latitude ionospheric convection and particle precipitation observations, several empirical models have been developed during the past several decades that provide distributions of the ionospheric convection and particle precipitation under certain conditions. For example, several particle precipitation models have been developed based on satellite observations (e.g., Fuller-Rowell & Evans, 1987; Hardy et al., 1987; Mitchell et al., 2013; Newell et al., 2009; Zhang & Paxton, 2008). Meanwhile, ionospheric convection models have been developed based on both satellite observations (e.g., Haaland et al., 2007; Heppner & Maynard, 1987; Papitashvili & Rich, 2002; Weimer, 2005) and ground-based measurements (e.g., Cousins & Shepherd, 2010; Foster et al., 1986; Holt et al., 1987; Ruohoniemi & Greenwald, 1996, 2005; Thomas & Shepherd, 2018; Zhang et al., 2007). Those models are highly valuable for the GCM modeling since they can be utilized either to directly drive GCMs or to set up the base for the data assimilation techniques, such as the Assimilative Mapping of Ionospheric Electrodynamics procedure (Richmond & Kamide, 1988), which can also be used to drive GCMs for event studies (e.g., Lu et al., 2016). However, a well-known issue in the GCM simulations is the inaccuracy in the Joule heating estimation when using models of large-scale convection and particle precipitation. In particular, the Joule heating is inadequate to reproduce observed ionospheric and thermospheric features during geomagnetic storms (e.g., Codrescu et al., 1995; Emery et al., 1999). The inaccuracy in the Joule heating estimation could be associated with a deficiency in empirical model specification of high-latitude electrodynamic forcing, and the binning methods used to develop those empirical models may contribute to this deficiency.

Typically, to develop an empirical model, the data from different times and under similar conditions are binned according to their magnetic local times (MLTs) and magnetic latitudes (MLATs), that is, in fixed geomagnetic coordinates. Hereafter, such a method is referred to as “static binning” method. However, it is likely that data from different source regions are combined in the same bin. For instance, the same geomagnetic location with fixed MLT and MLAT can be either inside and outside of the auroral oval due to the

dynamic nature of the auroral zone. Therefore, it is possible that particle precipitation measurements inside and outside the auroral oval are combined into the same bin when using the static binning method. Likewise, the electric field poleward or equatorward of the CRB can be mixed in the same bin. Therefore, the climatological patterns obtained through the static binning method can be smoothed and smeared (Chisham, 2017; Sotirelis & Newell, 2000).

To resolve the aforementioned issue caused by the static binning method, some studies have explored alternative binning approaches to process the ion convection and particle precipitation data (e.g., Chisham, 2017; Rich & Hairston, 1994; Sotirelis & Newell, 2000; Weimer, 2005). In those studies, the data are organized and binned according to certain boundaries instead of their MLATs and MLTs. In other words, the data are binned through the "boundary-oriented" binning method. For instance, Sotirelis and Newell (2000) binned particle precipitation data from the Defense Meteorological Satellite Program (DMSP) data set according to a sophisticated auroral boundary system, and they asserted some improvements in comparison with static patterns, although quantitative comparisons were lacking. As for the ion convection pattern, Heppner and Maynard (1987) presented average convection/potential patterns, based on manual alignment of DE-2 crossings. In their maps, the gradients near the CRB are much larger than in many modern models based on the static binning method. Later, Rich and Hairston (1994) organized the DMSP electric potential data according to the equatorward auroral boundary and Weimer (2005) organized the electric potential data from the Dynamic Explorer 2 (DE-2) satellite according to a low-latitude boundary. In those two studies, the location of the boundary is given by an empirical formula, which is a function of geomagnetic activity. Again, improvements have been claimed, but it is still unclear how significant the improvements are in terms of the distribution and magnitude of the electric potential. Recently, Chisham (2017) binned ionospheric vorticity data deduced from Super Dual Auroral Radar Network (SuperDARN) radars measurements according to the OCB determined from IMAGE FUV data. Their routines used to convert the measurements from geomagnetic coordinates to the OCB-oriented system are now available at a Python library (https://github.com/aburrell/ocbpy). Chisham (2017) compared patterns organized according to the OCB with the static patterns and found significant differences in the intensity and distribution.

While considerable efforts have been made to improve the accuracy of the specification of high-latitude-electrodynamic forcing, it is uncertain to what extent high-latitude ion convection and particle precipitation patterns differ between the static and boundary-oriented binning approaches. Meanwhile, it is not well established to what extent the Joule heating can be different if high-latitude ion convection and particle precipitation patterns obtained through different binning methods are utilized to drive a GCM. This study aims to address these questions: For the first question, DMSP electric potential and particle precipitation data are binned in both static and boundary-oriented binning approaches, and the quantitative comparisons between patterns obtained from both binning methods are provided. For the boundary-oriented binning approach, the particle precipitation data are organized according to the poleward and equatorward auroral boundaries to avoid mixtures of data inside and outside of the aurora zone. In addition, the electric potential data are organized according to the CRB to avoid mixtures of the ionospheric convection poleward and equatorward of the CRB. To address the second question, both static and boundary-oriented patterns are implemented in the Global Ionosphere and Thermosphere Model (GITM) to evaluate the impacts on Joule heating.

2. Data and Model

2.1. DMSP Data

In this study, particle precipitation and cross-track ion drift measurements from DMSP F16, F17, and F18 satellites from both hemispheres and during 2010–2014 are used. All three satellites flew in circular Sun-synchronous orbits at an altitude of ~840 km with an inclination of ~98.8°.

The particle precipitation data set utilized in this study is from the database created by Redmon et al. (2017) based on the measurements of the Special Sensor for Precipitating Particles, version 5 (SSJ5) onboard the DMSP satellites. The SSJ5 provides differential energy and number fluxes of precipitating electrons and ions in 19 logarithmically spaced energy channels from 30 eV to 30 keV every 1 s (Hardy et al., 2008; Redmon et al., 2017). The total energy (number) flux can be determined by integrating the differential energy (number) flux over different energy channels and multiplying by the factor of π if the downward differential particle energy (number) flux is assumed to be isotropic. The average energy is calculated from the ratio of

the total energy flux to the total number flux. We focused on the total energy flux and average energy of electron precipitation in this study.

The ion drift vector ($\mathbf{V}$) is measured by the Special Sensor for Ions, Electrons, and Scintillation (SSIES) every 1 s. After removing the spacecraft velocity with respect to the Earth and the velocity associated with the upper atmosphere's corotation with the Earth, the SSIES data set provides three components of the ion drift vector, V_x, V_y, and V_z, in the spacecraft coordinate system (i.e., $\mathbf{V}=V_x\,\hat{\mathbf{x}}+V_y\,\hat{\mathbf{y}}+V_z\,\hat{\mathbf{z}}$, where $\hat{\mathbf{x}}$ is along the satellite trajectory, $\hat{\mathbf{z}}$ is outward of the center of the Earth, and $\hat{\mathbf{y}}$ completes righthanded system). The cross-track ion drift vector ($\mathbf{V}_\perp$) used in this study consists of the V_y and V_z components. (i.e., $\mathbf{V}_\perp=V_y\,\hat{\mathbf{y}}+V_z\,\hat{\mathbf{z}}$). The SSIES is sensitive to the density and concentration of the O^+ in the ionosphere, and measurements are generally poor when the ionospheric O^+ density is low or other ion species (such as H^+) are dominant. Therefore, only measurements with a relatively high background O^+ concentration (>90%) and density ($>4\times10^3$ cm^{-3}) are utilized in this study. In addition, cross-track ion drift measurements from DMSP F17 satellite in 2010 and 2011 and from DMSP F18 satellite in 2010 are not reliable and are excluded in our data set. Since the CRB typically represents a large-scale phenomenon, a 500-km sliding window is applied to the original V_y and V_z data to remove small-scale structures at first. Then a linear baseline correction is applied to the smoothed data to ensure V_y and V_z are zero at the ends of the satellite pass (In this case,|MLAT|= 45°). The along-track electric field $\mathbf{E}_x$ ($\mathbf{E}_x=E_x\hat{\mathbf{x}}$) can be approximated through $\mathbf{E_x}\approx-\mathbf{V_y'}\times\mathbf{B_{0z}}$, where $\mathbf{V_y}'$ is the horizontal cross-track ion drift vector after applying the baseline correction and $\mathbf{B_{0z}}$ is the vertical component of the geomagnetic main field ($\mathbf{B_0}$) from the International Geomagnetic Reference Field-12 (IGRF-12) model (Thébault et al., 2015). The contribution of the vertical ion drift to E_x is generally small and therefore be neglected in our calculation. The along-track electric field is then integrated over the satellite pass to determine the electric potential along that pass. However, to obtain a reliable electric potential, the electric field and electric potential must both be zero at the ends of the satellite pass. The aforementioned baseline correction ensures the electric field being zero at the ends but does not necessarily lead to zero potentials at the ends. Thus, a correction proportional to $|E_x|$ is applied to E_x, that is, $E_x'=E_x+c|E_x|$, to ensure that the integration of E_x' along the whole polar pass (i.e.,|MLAT|> 45°) is zero. The correction factor c can be calculated as follows:

$$c=-\frac{\int_s^f E_x\,dx}{\int_s^f |E_x|dx} \tag{2}$$

Here s and f denote the start and final points of the pass and dx is the distance between two consecutive measurements. The tracks of which |c|> 0.4 are excluded in this study, in order to effectively remove the passes during which the IMF conditions have a significant temporal change. Then it is assumed that E_x' is only contributed by a corrected ion drift along the $\hat{\mathbf{y}}$ direction, and the corrected V_y can be calculated accordingly. Both the electric potential and ion drift V_y component calculated from the E_x' are utilized in section 3.

2.2. IMF Data

Two parameters of the IMF data are used to categorize the geomagnetic conditions: (1) the IMF transverse component magnitude, B_t, which represents the strength of the IMF projection onto the geocentric solar magnetospheric (GSM) *Y-Z* plane, that is, $B_t=\sqrt{B_y^2+B_z^2}$; 2) IMF clock angle (θ), which stands for the angle between GSM north and the IMF projection onto the GSM *Y-Z* plane and is given by $\theta=\mathrm{atan2}(B_y,B_z)$. (Note that the subscripts y and z have different meanings in this subsection than in the previous subsection.) The IMF data used in this study are 5-min-averaged data from Space Physics Data Facility OMNIWeb interface based on the measurements from ACE and WIND satellites. We shifted the IMF data by 30 min in order to account for the time delay between IMF changes at the bow shock and geomagnetic effects in the ionosphere. In this study, we have specifically focused on the dominantly southward IMF conditions, which satisfy the following criteria during the polar crossing: the IMF clock angle is between 135° and 225° and the average of available 5-min B_t data during the crossing period is between 3 and 10 nT with the standard deviation of available 5-min B_t data during the crossing period smaller than 1.2 nT.

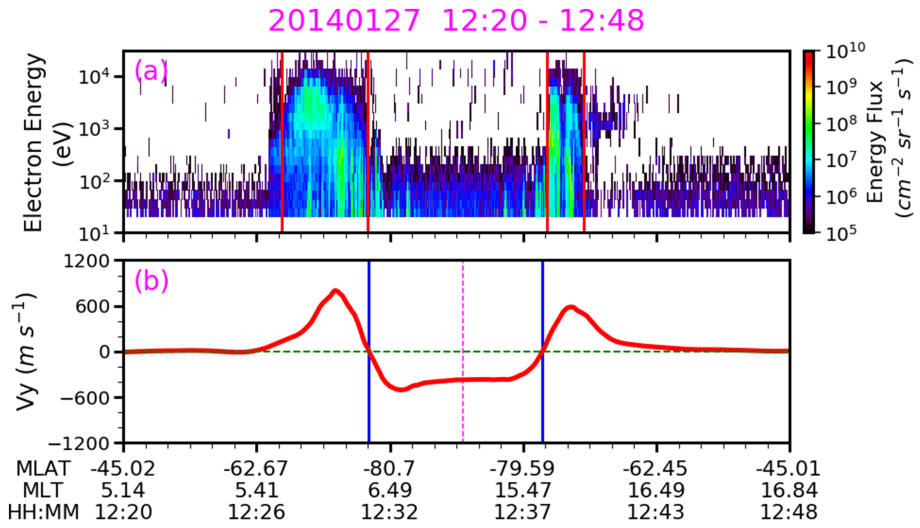

Figure 1. (a) The electron energy spectrogram from a DMSP F16 polar trajectory in the Southern Hemisphere and (b) the horizontal cross-track ion drift (V_y) measurements smoothed by a 500-km moving average window along the same trajectory. Vertical red lines in Figure 1a and vertical blue lines in Figures 1b denote the auroral boundaries and convection reversal boundaries (CRBs) along this trajectory, respectively. Vertical magenta dashed line in Figure 1b denotes the zero-potential point of this trajectory.

2.3. GITM

GITM is a three-dimensional spherical model for the Earth's thermosphere and ionosphere system (Ridley et al., 2006). The density, velocity, and temperature of neutrals, ions, and electron can be solved self-consistently in GITM. The grid size option is flexible and the latitudinal and altitudinal grids can be stretched. Moreover, by virtue of the relaxation the hydrostatic assumption, it can evaluate non-hydrostatic effects on the I-T system (e.g., Deng et al., 2008, 2011; Lin et al., 2017; Zhu et al., 2017). More details about GITM can be found in Ridley et al. (2006).

The Joule heating deposition rate in GITM is calculated by using equation (1). The electric field is determined from the statistical binning analysis of the electric potential data, and the neutral wind is self-consistently calculated by GITM. The total electron energy flux and average energy are used to calculate the ionization rate due to the particle precipitation by using the formulation described by Frahm et al. (1997) and the partitioning of ionization rates among O^+, $O_2{}^+$, and $N_2{}^+$ described in Rees (1989). The ionization due to the solar radiation in GITM is specified by chemical reactions in Rees (1989) or Torr et al. (1979). With these, the electron and ion densities are calculated from the continuity equations and the conductivity is calculated using the electron and ion densities, geomagnetic field, and collision frequencies.

3. Results and Discussion

3.1. Comparisons of Results Obtained From Different Binning Methods: Electron Precipitation

3.1.1. Auroral Boundary Identification

Figure 1a represents the electron energy spectrogram along a DMSP F16 polar pass in the Southern Hemisphere. Overplotted red lines indicate the auroral boundaries identified along this track by using the technique developed by Kilcommons et al. (2017) for the particle data, which is an improved version of the technique developed by Redmon et al. (2010). The first step of this technique is to identify all aurora region candidates on both dawnside and duskside that correspond to regions where the integrated energy flux for electron above 1 kV is continuously above an empirical threshold (10^9 eV/cm^2/s/sr). Then a figure of merit (FOM) is used to rate the likelihood of a pair of the candidate regions (one on the dawnside and the other on the duskside) being main auroral ovals, and the pair of regions with a highest FOM is defined as the main auroral ovals. However, if the highest FOM is smaller than 3, the track is excluded. The poleward and equatorward boundaries of the main auroral oval can be determined accordingly. More details about how the FOM is calculated and how the main auroral ovals are selected can be found in Kilcommons

et al. (2017), and their codes are now available in Kilcommons and Burrell (2019). We have collected ~3,100 tracks with auroral boundaries identified under the IMF conditions considered in this study.

The top panel of Figure 2 shows distributions of the auroral boundaries that were identified in the data set as a function of MLAT and MLT. Different colors correspond to different satellites. To achieve a better data coverage, boundaries from both hemispheres and all seasons are combined. It is clear that the most poleward auroral boundaries (PABs) are located within 70°~80°|MLAT|and most equatorward auroral boundaries (EABs) are mainly located within 60°–70°|MLAT|. The bottom panel of Figure 2 displays distributions of the median MLAT of the corresponding boundary in each 0.5-hr MLT bin. Only medians in bins where the number of boundaries is greater than 30 are calculated, as indicated by the red dots. For bins without sufficient data, the median locations are obtained through an elliptical fitting based on the red dots, as indicated by blue plus signs. The median PAB is close to a circle, of which the center has a small offset (~1°) from the geomagnetic pole, while the median EAB tends to be more elliptical. Overall, the general characteristics of the auroral boundaries are consistent with previous studies under moderately disturbed geomagnetic conditions (e.g., Feldstein & Starkov, 1967; Sotirelis & Newell, 2000).

3.1.2. Boundary-Oriented Binning Approach

In this study, similar approaches used in Kilcommons et al. (2017) and Redmon et al. (2010) have been adopted to organize the particle precipitation data according to auroral boundaries. First, the high-latitude region is divided into three zones: (1) poleward of the auroral zone (PZ): $|\mathrm{MLAT}_{\mathrm{PAB}}| \le |\mathrm{MLAT}| \le 90°$; (2) auroral zone (AZ):$|\mathrm{MLAT}_{\mathrm{EAB}}| \le |\mathrm{MLAT}| < |\mathrm{MLAT}_{\mathrm{PAB}}|$; and (3) equatorward of the auroral zone (EZ): $45° \le |\mathrm{MLAT}| < |\mathrm{MLAT}_{\mathrm{EAB}}|$. Here $\mathrm{MLAT}_{\mathrm{PAB}}$ and $\mathrm{MLAT}_{\mathrm{EAB}}$ are MLATs of the PAB and EAB, respectively. Second, we calculated the fractional distances of the measurements (L) in corresponding regions, which can be expressed as follows:

$$\mathrm{L_{PZ}} = \frac{|\mathrm{MLAT^m}| - |\mathrm{MLAT^m_{PAB}}|}{90° - |\mathrm{MLAT^m_{PAB}}|} \quad |\mathrm{MLAT^m_{PAB}}| \le |\mathrm{MLAT^m}| \le 90° \tag{3}$$

$$\mathrm{L_{AZ}} = \frac{|\mathrm{MLAT^m}| - |\mathrm{MLAT^m_{EAB}}|}{|\mathrm{MLAT^m_{PAB}}| - |\mathrm{MLAT^m_{EAB}}|} \quad |\mathrm{MLAT^m_{EAB}}| \le |\mathrm{MLAT^m}| < |\mathrm{MLAT^m_{PAB}}| \tag{4}$$

$$\mathrm{L_{EZ}} = \frac{|\mathrm{MLAT^m}| - 45°}{|\mathrm{MLAT^m_{EAB}}| - 45°} \quad 45° \le |\mathrm{MLAT^m}| < |\mathrm{MLAT^m_{EAB}}| \tag{5}$$

Here $\mathrm{MLAT^m}$ represents the MLAT of a measurement, $\mathrm{MLAT^m_{PAB}}$ and $\mathrm{MLAT^m_{EAB}}$ are the MLATs of the identified PAB and EAB on the side of the track where the measurement is taken, respectively.

The data are mapped latitudinally according to the statistical locations of the equatorward and poleward boundaries of the region where the data is located and the fractional distance relative to those boundaries. The modified magnetic latitude after mapping ($\mathrm{MLAT^n}$) in different regions can be expressed as follows:

$$\mathrm{MLAT^s_{PAB}} + \mathrm{L_{PZ}} \times \left(90° - \mathrm{MLAT^s_{PAB}}\right), \text{if in the PZ} \tag{6}$$

$$\mathrm{MLAT^s_{EAB}} + \mathrm{L_{AZ}} \times \left(\mathrm{MLAT^s_{PAB}} - \mathrm{MLAT^s_{EAB}}\right), \text{if in the AZ} \tag{7}$$

$$45° + \mathrm{L_{EZ}} \times \left(\mathrm{MLAT^s_{EAB}} - 45°\right), \text{if in the EZ} \tag{8}$$

$\mathrm{MLAT^s_{PAB}}$ and $\mathrm{MLAT^s_{EAB}}$ represent median MLATs of the PAB and EAB in the corresponding MLT bin. Then the mapped data are binned according to its MLT and modified MLAT.

3.1.3. Static Versus Boundary-Oriented Binning Results

Figure 3 summarizes the averages of the total electron energy flux and average electron energy in each bin as a function of MLT and MLAT obtained through different binning approaches. The bin size is 1 hr in MLT by 1° in MLAT, and grey-shaded areas indicate bins without sufficient data point (<400). Figures 3a and 3b depict the static total electron energy flux and average electron energy patterns. The total energy flux shows a horseshoe shape that is roughly symmetric about the 1–13 MLT meridian and is generally 2–3 erg $\mathrm{cm^{-2}\,s^{-1}}$ on the night side. Meanwhile, the maximum of the average energy is located on the morning side. The

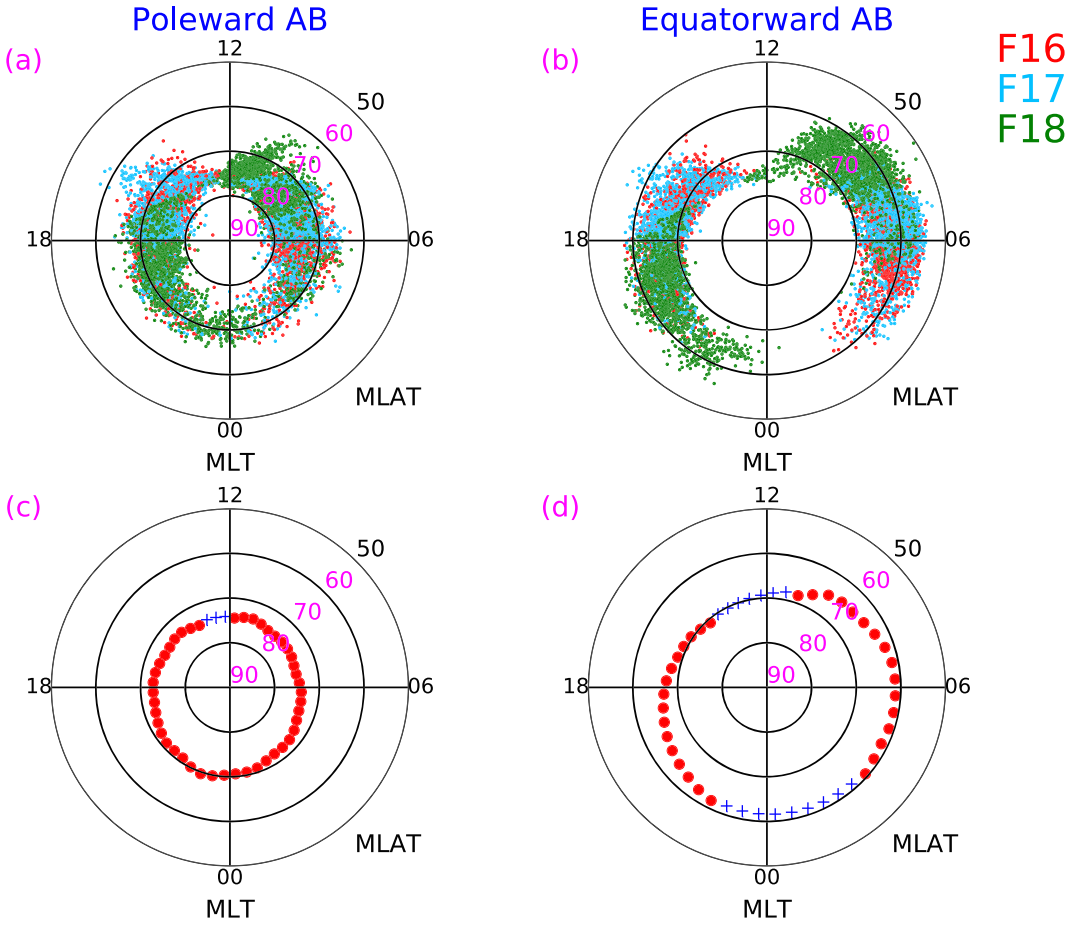

Figure 2. Scatters of (a) poleward auroral boundary and (b) equatorward auroral boundary identified under moderately strong and dominant southward interplanetary magnetic field (IMF) conditions as a function of magnetic local time (MLT) and magnetic latitude (MLAT). Different colors denote different satellites (Red: F16, Blue: F17, and Green: F18); (bottom) distributions of the median MLAT of (c) poleward auroral boundary and (d) equatorward auroral boundary. Red dots indicate bins with sufficient boundaries whereas blue plus signs suggest bins without enough boundaries and represent fitted MLATs.

general behaviors are similar to those shown in previous studies under moderately disturbed conditions (e.g., Fuller-Rowell & Evans, 1987; Hardy et al., 1987; Newell et al., 2009; Zhang & Paxton, 2008). Figures 3c and 3d exhibit the total energy flux and average energy patterns obtained from the boundary-oriented approach. The average energy pattern (Figure 3d) seems to be similar to the static pattern (Figure 3b), where the maximum is still located on the morning side but its magnitude increases by 10%–20%. However, the peak total energy fluxes are more intense in the 14–24 MLT sector than the 2–12 MLT sector as shown in Figure 3c, which is not captured by the static pattern (Figure 3a). Our results are consistent with the boundary-oriented patterns shown in Sotirelis and Newell (2000) under moderately disturbed conditions, although a more sophisticated boundary was utilized in their study. In addition, the total energy fluxes in the statistical auroral zone (regions enclosed by red dashed lines) tend to be higher in the boundary-oriented pattern (Figure 3c) than those in the static pattern (Figure 3a). The enhancements are more substantial in the 14–24 MLT sector than those in 2–12 MLT sector. More specifically, the enhancements of the peak magnitude in the 14–24 MLT sector can exceed 50% of the peak magnitude in the static binning results, while the enhancements of the peak magnitude in 2–12 MLT are smaller than 25% of the peak magnitude in the static binning results in general.

Figure 4 provides detailed comparisons of the latitudinal profiles of different parameters from different binning results at 5 and 6 and 17 and 18 MLT sectors. The difference in responses of the total energy flux to the

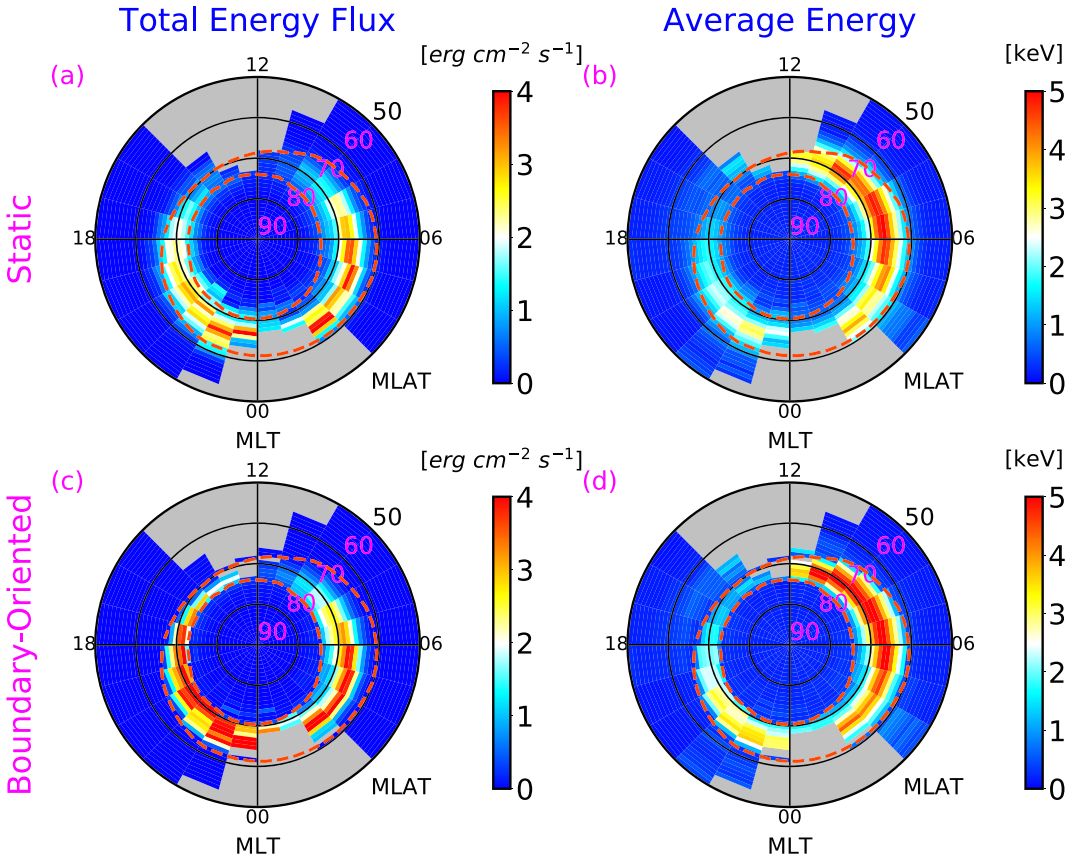

Figure 3. (top) Static and (bottom) Boundary-oriented binning results for (left) total electron energy flux and (eight) average electron energy. Red dashed lines stand for statistical locations of the auroral boundaries. Grey shaded areas indicate regions without enough data. All plots are presented in geomagnetic coordinates.

binning methods on dawnside and duskside identified in Figure 3 can also be seen in Figures 4a and 4c. Clearly, the changes in the latitudinal profiles on the dawnside (Figure 4a) are not as dramatic as those on the duskside (Figure 4c). On the duskside, the full width at half maximum of the latitudinal profile obtained from the boundary-oriented binning approach is ~50% smaller than that from the static binning approach, while the peak magnitude undergoes a ~80% elevation. Similar differences can also be seen in the latitudinal profiles along other meridians (not shown here), indicating that the boundary-oriented binning method can lead to a particle precipitation pattern with significantly sharper transitions near the auroral boundaries on the duskside. On the duskside, the relatively intense and dynamic monoenergetic electron precipitation frequently occurs (e.g., Newell et al., 2009). The significant increase of the peak total energy flux on the duskside from the boundary-oriented binning method suggests that the boundary-oriented binning method may better represent the contribution of the monoenergetic electron precipitations than the static binning method. Meanwhile, the fact that substorms occur more frequently on the duskside and that the static binning method cannot well capture these rapid expansions/contractions might also contribute to the larger differences between the static and boundary-oriented patterns on the duskside.

3.2. Comparisons of Results Obtained From Different Binning Methods: Electric Potential

3.2.1. CRB Identification

Figure 1b shows the smoothed and corrected horizontal cross-track ion drift (V_y) measurements along the same trajectory as shown in Figure 1a, which is utilized to identify CRBs. The technique used in this study is similar to that used in Chen et al. (2015), which aims to search locations of the reversal points of V_y, as indicated by blue lines in Figure 1b. The CRBs identified through the method developed by Chen et al. (2015) are statistically found to be in good agreement with the OCBs identified through a recently developed method

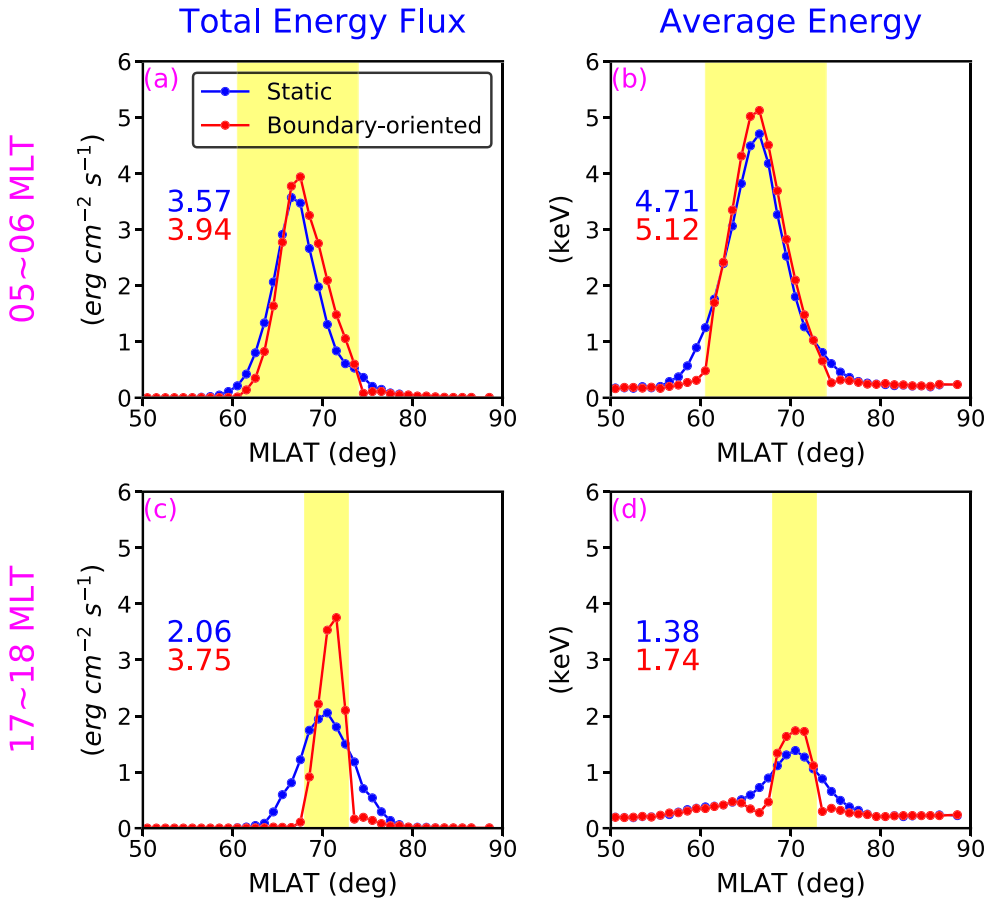

Figure 4. Comparisons of latitudinal profiles of (left) total electron energy flux and (right) average electron energy obtained through different binning methods in (top) 5–6 and (bottom) 17–18 MLT sectors. Blue and red lines denote static and boundary-oriented binning results, respectively. Yellow-shaded areas correspond to the auroral zone. The numbers in each plot represent the values of the maximum magnitude of the static (blue) and boundary-oriented (red) profiles.

based on the Active Magnetosphere and Planetary Electrodynamics Response Experiment magnetic perturbation observations (Burrell et al., 2019). Although the example shown in Figure 1b is quite straightforward, it is worth noting that the configuration of the convection pattern and its relationship with the configuration of satellite trajectory can bring in more complexities for CRB identification (Chen et al., 2015). For instance, it is possible that more than two CRBs are encountered along a trajectory owing to the appearance of a multicell convection pattern. It is also possible that no CRB can be identified along a track since the convection pattern is relatively small and the satellite does not cross it. In this study, all tracks with two CRBs identified are included and all tracks with no CRB identified are excluded. For other cases, if a single zero-potential point can be found between the potential maximum and minimum (also should be extrema) and if a single CRB can be identified on one side of the zero-potential point, the corresponding part of the track is kept; otherwise, the whole track is discarded. We have collected approximately 2,000 tracks with CRB identified under moderately strong and dominant southward IMF conditions. In this study, it is not required that the CRBs and auroral boundaries are identified simultaneously along the same trajectory; otherwise, the number of available trajectories would be substantially reduced and would not have a good coverage near noon and midnight.

3.2.2. Boundary-Oriented Binning Approach

In this and following paragraphs, we illustrate how to organize the electric potential data from a geomagnetic coordinate to CRB-oriented coordinate referenced to a reference CRB (obtained as described in section 3.2.3) and to a reference zero-potential line. Figure 5a shows the locations of zero-potential points of all the individual passes and the reference zero-potential line fitted to these points. As in Hairston and

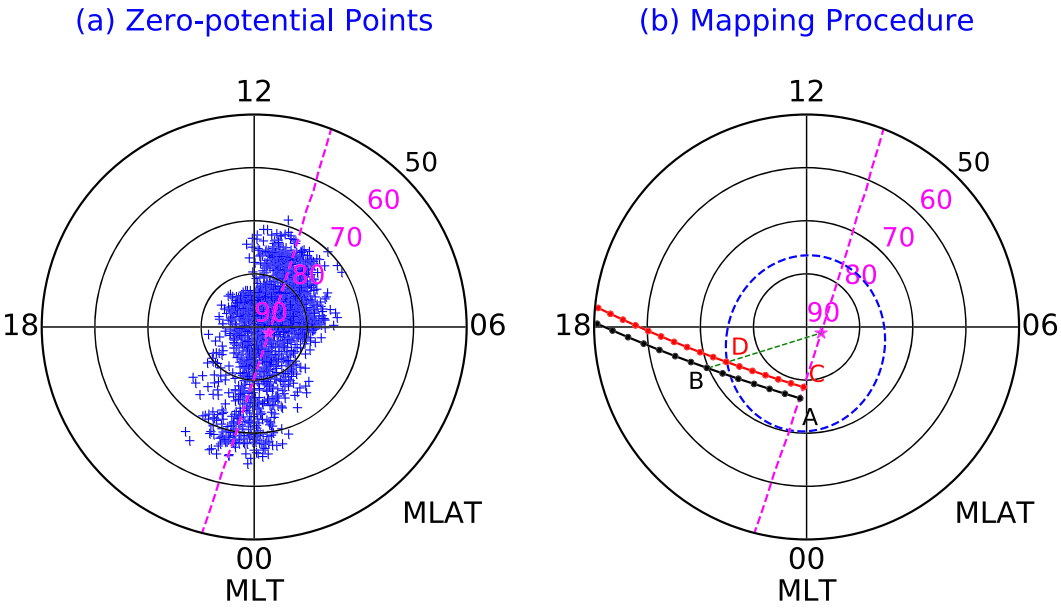

Figure 5. (a) Distributions of the zero-potential points identified under moderately strong and dominant southward interplanetary magnetic field (IMF) conditions as a function of magnetic local time (MLT) and magnetic latitude (MLAT). Magenta dashed line indicates the best-fit parabola of the zero-potential points and the magenta star denotes the vertex of the parabola. (b) An example to illustrate how to organize electric potential data according to the CRB. Blue dashed line indicates the location of the reference CRB. The black dotted line indicates the trajectory after the minimum displacement that makes its zero-potential point lie on the parabola. The red dotted line indicates the mapped trajectory, involving a further displacement as well as a contraction or elongation to make the CRB for that pass lie on the reference CRB. See text for more details.

Heelis (1990), the reference zero-potential line is defined as a parabola with the equation $\beta = c_1\alpha^2 + c_2$. The α axis is defined as a straight line fitted to the collection of zero-potential points and the β axis is orthogonal to this, passing through the pole. The constants c_1 and c_2 are found by least squares fitting to the points. Each individual pass is then adjusted such that its zero-potential point lies on the zero-potential line and its maximum or minimum potential lies on the dawnside or duskside reference CRB, respectively, in order to avoid mixing data from the positive and negative potential cells.

With reference to Figure 5b, the adjustments are carried out as follows. First, each track included in our data set is displaced by the minimum distance that brings its zero-potential point (point A) to lie on the zero-potential parabola, with the displaced track (black dotted line) remaining parallel to the original. Next, we draw a line (green dashed) from the extremum potential of the displaced track (point B) to the vertex of the parabola (magenta star), which lies near the center of the convection pattern. We then displace the track again and contract or elongate it such that its potential extremum (point D) lies on the intersection of the green line with the statistical CRB (blue ellipse) and its zero-potential point (point C) is shifted along the reference zero-potential parabola, with the displaced track (red dotted line) remaining parallel to the original. The potential data on the mapped track are subsequently binned with respect to the modified MLAT and MLT.

3.2.3. Static Versus Boundary-Oriented Binning Results

Figures 6a shows the electric potential pattern obtained from the static binning method, which exhibits a clear two-cell pattern and is consistent with those obtained by previous studies (e.g., Thomas & Shepherd, 2018, and references therein). The red dashed ellipse in Figure 6a denotes the best-fit ellipse of locations of the maximum electric potential magnitude at different MLTs, which is used as the reference CRB for the boundary-oriented binning method as shown in Figure 5b. The electric potential pattern obtained from the boundary-oriented binning method is shown in Figure 6b, which does not exhibit significant changes in the overall pattern. However, in comparison with the static pattern, the cross polar cap potential (CPCP) increases from 65.07 to 72.47 kV (~11%). Moreover, as revealed by the latitudinal profiles of the electric potential on the dawnside and duskside (Figures 6c and 6d), the boundary-oriented binning approach

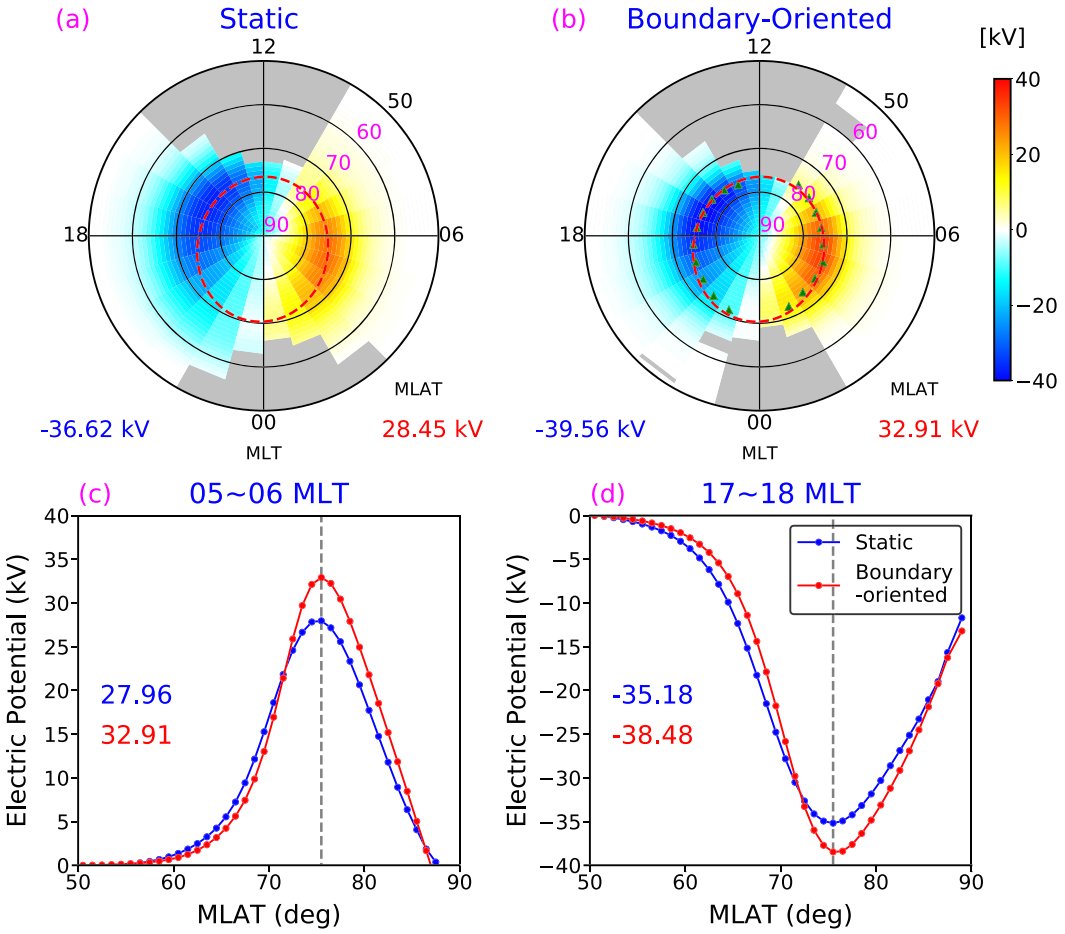

Figure 6. (top) Electric potential pattern derived from the (a) static and (b) boundary-oriented binning methods, respectively. The potential maximum and minimum for each pattern are labeled at the bottom right and left sides of plots (a) and (b), respectively. Red dashed line in Figures 6a and 6b denotes the location of the reference CRB. Green triangles in Figure 6b denotes the unbiased CRB. Grey shaded areas indicate regions without enough data. Both plots are presented in geomagnetic coordinates; (bottom) comparisons of latitudinal profiles of electric potential obtained through different binning methods in (c) 5 and 6 and (d) 17 and 18 MLT sectors. The grey dashed lines correspond to the convection reversal boundary. The numbers in both plots represent the values of the maximum magnitude of the static (blue) and boundary-oriented (red) profiles.

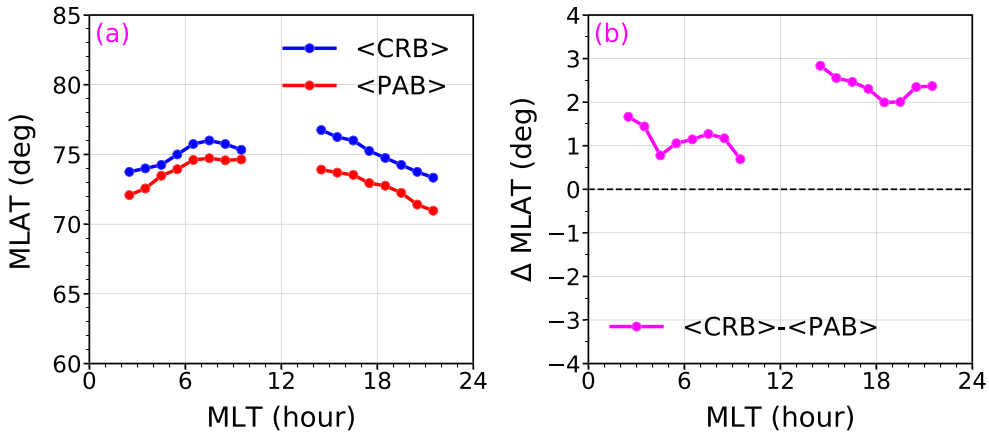

Figure 7. (a) Distributions of the magnetic latitudes (MLATs) of the unbiased CRB and average PAB as a function of magnetic local time (MLT) (b) MLAT offsets between the locations of the unbiased CRB and average PAB as a function of MLT.

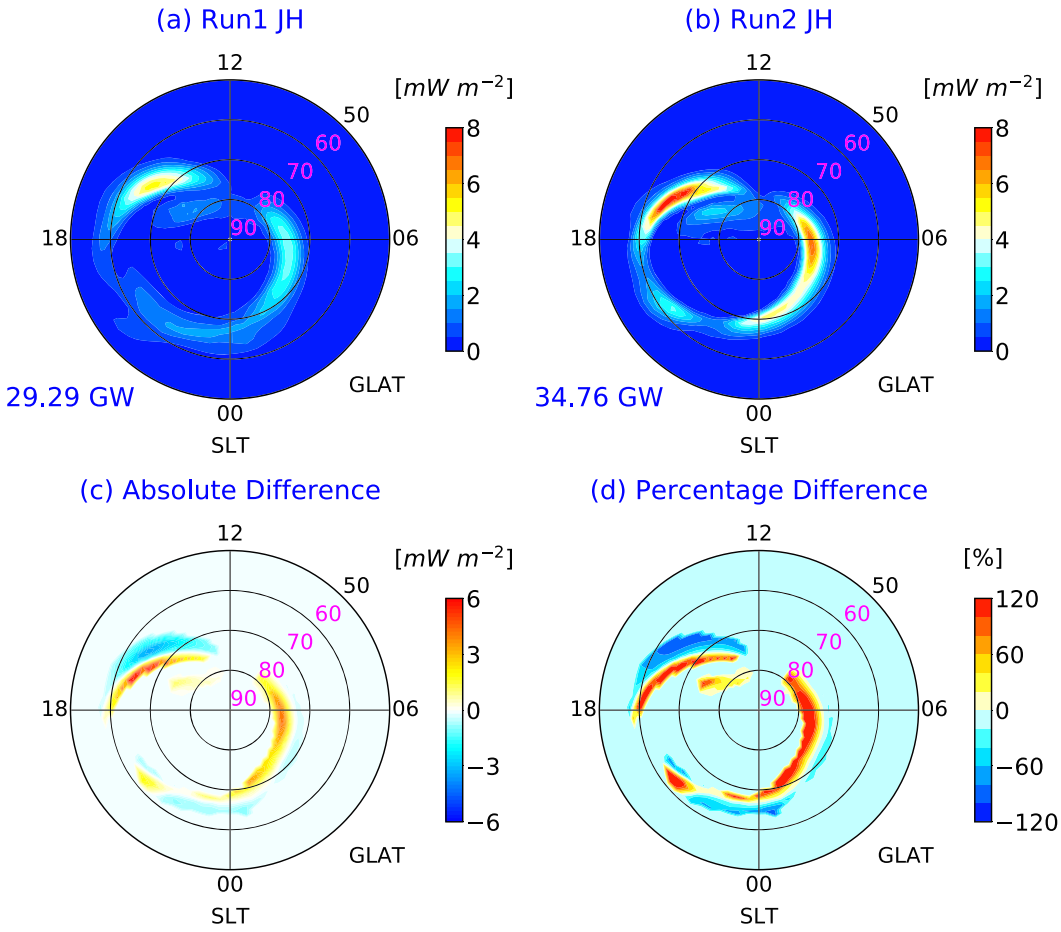

Figure 8. (a) Distribution of the height-integrated Joule heating from Run 1; (b) distribution of the height-integrated Joule heating from Run 2. The hemispherical-integrated Joule heating is denoted at the left bottom of each plots. (c) Absolute difference of the height-integrated Joule heating between Runs 2 and 1 (Run 2–Run 1); (d) percentage difference of the height-integrated Joule heating between Runs 2 and 1 ((Run 2–Run 1)/Run 1 × 100). All plots are presented in geographic coordinates.

also tends to increase the magnitude of the electric potential gradient (i.e., the electric field) near the CRB. Therefore, it implies that the boundary-oriented pattern may be better able than the static pattern to capture the sharp transitions of the cross-track ion drift near the CRB that are typically shown in the observations (e.g., Figure 11c in Weimer, 2005).

From the boundary-oriented binning pattern, the unbiased CRB can be determined by finding the MLAT of the maximum electric potential magnitude at each MLT, as indicated by the green triangles in Figure 6b. Figure 7 provides a comparison between the locations of the average PAB and the unbiased CRB on the dawnside (2–10 MLT) and duskside (14–22 MLT). Clearly, the separation between CRB and PAB is generally small, suggesting a good alignment between the PAB and CRB. More specifically, the separations are relatively smaller on the dawnside (<2°) in comparison with those on the duskside (<3°) as shown in Figure 7b. Previous studies based on ground-based SuperDARN radar and DMSP particle precipitation measurements (e.g., Newell et al., 2004; Sotirelis et al., 2005) indicate that there is a good alignment between OCB and CRB. Given the good alignment between OCB and PAB (Newell et al., 1996), our results are qualitatively consistent with previous results, although quantitative discrepancies could exist owing to the differences in the CRB and auroral boundary identification techniques used in our study and previous studies. For example, the auroral region identified in this study is dependent on a threshold total energy flux level for electrons above 1 keV and may not well capture the low-latitude boundary layer, of which the poleward edge is usually found to be collocated with the OCB (Drake et al., 2009). Thus, while the auroral boundary locations are useful to determine the impacts on the ionosphere and thermosphere, the location

of particle sources in the magnetosphere may not be well identified with the auroral boundary identification technique used in this study.

3.3. Impacts on Joule Heating by Using Patterns From Different Binning Methods

In sections 3.2.2 and 3.2.3, we have applied both static and boundary-oriented binning approaches to bin the particle precipitation and electric potential data. As compared with the static binning results, the boundary-oriented binning approach results in stronger changes in the particle precipitation on the duskside, whereas the changes on the dawnside are relatively modest. Meanwhile, the CPCP as well as the magnitude of the electric potential gradient (i.e., electric field) near the CRB increase on both dawnside and duskside. As expected, changes in the localized Joule heating would occur if a GCM is driven by results from different binning methods. However, it is still unclear to what degree the Joule heating peak values would change on dawnside and duskside. Moreover, it still remains unknown whether the hemispheric-integrated Joule heating would undergo a significant change when a GCM is driven by results from different binning methods. Quantitative investigations are provided in this subsection to shed light on those questions.

In this study, two simulations are carried out: Run 1 is a reference run, where the high-latitude forcing of GITM is specified by the static binning results (Figures 3a, 3b, and 6a); in Run 2, the high-latitude forcing of GITM is specified by the boundary-oriented binning results (Figures 3c, 3d, and 6b). The data gaps (grey-shaded areas) at noon and midnight are filled by applying a linear interpolation based on values in adjacent bins. The patterns are then smoothed in MLT and MLAT directions. The spatial resolution for all simulations is 5° in longitude by 1° in latitude and 1/3 scale height in altitude. The temporal resolution is 2 s. All simulations are conducted under moderate solar activity ($F_{10.7} = 120$ sfu) and at the September equinox. In addition, a 24-hr prerun (00 UT on 22 September 2002 to 00 UT on 23 September 2002) has been carried out, so that the neutral dynamics in GITM reach a quasi-steady state when the simulations are conducted.

Figures 8a and 8b summarize outputs of the height-integrated Joule heating from both runs at 10 min after the prerun (i.e., 00:10:00 UT on 23 September 2002), As compared with the case when GITM is driven by static patterns (Figure 8a), the GITM simulation driven by the boundary-oriented patterns (Figure 8b) shows larger height-integrated Joule heating peaks on both dawnside and duskside, although they tend to be located at higher latitudes (Figures 8c and 8d). The peak values of Joule heating in Run 2 increases by 112% and 94% as compared with Run 1 on dawnside and duskside, respectively. However, even though the regions with intense height-integrated Joule heating are located at higher latitudes in Run 2, the hemispheric-integrated Joule heating still increases from 29.29 to 34.76 GigaWatt (GW) (18%), which is not negligible.

4. Summary

In this study, electron precipitation and electric potential data from the DMSP satellites are analyzed under conditions when IMF is moderately strong and dominantly southward. First, statistical MLATs of auroral boundaries and CRB as a function of MLT have been investigated. Second, the particle precipitation and electric potential data are binned through static and boundary-oriented methods and the results are compared quantitatively. Finally, both static and boundary-oriented binning results are utilized to drive GITM in order to assess the impacts of the electrodynamic forcing patterns obtained from different binning methods on Joule heating. The primary findings are as follows:

1. The CRB is well aligned with the poleward auroral boundary (<3° separations in general).
2. In comparison with the static binning results, the boundary-oriented binning method significantly changes the morphology of the electron precipitation which is more predominant on the duskside. In addition, the boundary-oriented binning method increases the CPCP by 11% and the magnitude of the electric potential gradient (electric field) near the CRB.
3. As compared with the case in which GITM is driven by static patterns, GITM simulation driven by the boundary-oriented patterns shows an 18% increase of the hemispheric-integrated Joule heating, even though the regions with intense height-integrated Joule heating are more poleward.

Acknowledgments
The research at University of Texas at Arlington was supported by NASA through grants NNX14AD46G and AFOSR through awards FA9550-16-1-0059 and FA9559-16-1-0364. A. M. and A. D. R. were supported by AFOSR through award FA9559-17-1-0248. Y. J. C. is supported by AFOSR award FA9559-16-1-0364. M. R. H. is supported by NSF grants AGS-1552245 and NNX15AT31G. D. J. K. and L. M. K. were partially supported by AFOSR award FA9550-17-1-0258 and by subcontract award 26-0201-51-64 from AFOSR MURI award to University of Texas at Arlington. This material is based upon work supported by the National Center for Atmospheric Research, which is a major facility sponsored by the NSF under cooperative agreement 1852977. The DMSP particle precipitation data and auroral boundary information can be found at NASA SPDF CDAWeb (https://cdaweb.sci.gsfc.nasa.gov/index.html/) and the DMSP cross-track ion drift data can be obtained at NOAA NCEI (https://satdat.ngdc.noaa.gov/dmsp/data/). The IMF data are downloaded from NASA SPDF OMNIWeb (https://omniweb.gsfc.nasa.gov). The authors acknowledge the Texas Advanced Computing Center at the University of Texas at Austin for providing High-performance computing (HPC) and visualization resources that have contributed to the research results reported within this paper (http://www.tacc.utexas.edu). The modeling results and processed data used for this paper are stored at http://doi.org/10.5281/zenodo.3530610.

References

Akasofu, S. I. (1964). The development of the auroral substorm. *Planetary and Space Science*, *12*(4), 273–282. https://doi.org/10.1016/0032-0633(64)90151-5

Baker, J. B., Clauer, C. R., Ridley, A. J., Papitashvili, V. O., Brittnacher, M. J., & Newell, P. T. (2000). The nightside poleward boundary of the auroral oval as seen by DMSP and the Ultraviolet Imager. *Journal of Geophysical Research*, *105*(A9), 21,267–21,280. https://doi.org/10.1029/1999JA000363

Bristow, W. A., & Spaleta, J. (2013). An investigation of the characteristics of the convection reversal boundary under southward interplanetary magnetic field. *Journal of Geophysical Research: Space Physics*, *118*, 6338–6351. https://doi.org/10.1002/jgra.50526

Burch, J. L., Reiff, P. H., Menietti, J. D., Heelis, R. A., Hanson, W. B., Shawhan, S. D., et al. (1985). IMF B_y-dependent plasma flow and Birkeland currents in the dayside magnetosphere: 1. Dynamics Explorer observations. *Journal of Geophysical Research*, *90*(A2), 1577–1593. https://doi.org/10.1029/JA090iA02p01577

Burrell, A. G., Chisham, G., Milan, S. E., Kilcommons, L., Chen, Y.-J., Thomas, E. G., & Anderson, B. (2019). Ampere polar cap boundaries. *Annales Geophysicae Discussions*, *2019*, 1–16. https://doi.org/10.5194/angeo-2019-113

Chen, Y.-J., & Heelis, R. A. (2018). Motions of the convection reversal boundary and local plasma in the high-latitude ionosphere. *Journal of Geophysical Research: Space Physics*, *123*, 2953–2963. https://doi.org/10.1002/2017JA024934

Chen, Y.-J., Heelis, R. A., & Cumnock, J. A. (2015). Response of the ionospheric convection reversal boundary at high latitudes to changes in the interplanetary magnetic field. *Journal of Geophysical Research: Space Physics*, *120*, 5022–5034. https://doi.org/10.1002/2015JA021024

Chisham, G. (2017). A new methodology for the development of high-latitude ionospheric climatologies and empirical models. *Journal of Geophysical Research: Space Physics*, *122*, 932–947. https://doi.org/10.1002/2016JA023235

Codrescu, M. V., Fuller-Rowell, T. J., & Foster, J. C. (1995). On the importance of *E*-field variability for Joule heating in the high-latitude thermosphere. *Geophysical Research Letters*, *22*, 2393–2396. https://doi.org/10.1029/95GL01909

Cousins, E. D. P., & Shepherd, S. G. (2010). A dynamical model of high-latitude convection derived from SuperDARN plasma drift measurements. *Journal of Geophysical Research*, *115*, A12329. https://doi.org/10.1029/2010JA016017

de la Beaujardiere, O., Alcayde, D., Fontanari, J., & Leger, C. (1991). Seasonal dependence of high-latitude electric fields. *Journal of Geophysical Research*, *96*(A4), 5723–5735. https://doi.org/10.1029/90JA01987

Deng, Y., Fuller-Rowell, T. J., Akmaev, R. A., & Ridley, A. J. (2011). Impact of the altitudinal Joule heating distribution on the thermosphere. *Journal of Geophysical Research*, *116*, A05313. https://doi.org/10.1029/2010JA016019

Deng, Y., Richmond, A. D., Ridley, A. J., & Liu, H.-L. (2008). Assessment of the non- hydrostatic effect on the upper atmosphere using a general circulation model (GCM). *Geophysical Research Letters*, *35*, L01104. https://doi.org/10.1029/2007GL032182

Ding, G.-X., He, F., Zhang, X.-X., & Chen, B. (2017). A new auroral boundary determination algorithm based on observations from TIMED/GUVI and DMSP/SSUSI. *Journal of Geophysical Research: Space Physics*, *122*, 2162–2173. https://doi.org/10.1002/2016JA023295

Drake, K. A., Heelis, R. A., Hairston, M. R., & Anderson, P. C. (2009). Electrostatic potential drop across the ionospheric signature of the low-latitude boundary layer. *Journal of Geophysical Research*, *114*, A04215. https://doi.org/10.1029/2008JA013608

Dungey, J. W. (1961). Interplanetary magnetic field and the auroral zones. *Physical Review Letters*, *6*(2), 47–48. https://doi.org/10.1103/PhysRevLett.6.47

Emery, B. a., Lathuillere, C., Richards, P. G., Roble, R. G., Buonsanto, M. J., Knipp, D. J., et al. (1999). Time dependent thermospheric neutral response to the 2–11 November 1993 storm period. *Journal of Atmospheric and Terrestrial Physics*, *61*(3-4), 329–350. https://doi.org/10.1016/S1364-6826(98)00137-0

Feldstein, Y. I., & Starkov, G. V. (1967). Dynamics of auroral belt and polar geo magnetic disturbances. *Planetary and Space Science*, *15*, 209–229. https://doi.org/10.1016/0032-0633(67)90190-0

Foster, J. C., Holt, J. M., Musgrove, R. G., & Evans, D. S. (1986). Ionospheric convection associated with discrete levels of particle precipitation. *Geophysical Research Letters*, *13*, 656–659. https://doi.org/10.1029/GL013i007p00656

Frahm, R. A., Winningham, J. D., Sharber, J. R., Link, R., Crowley, G., Gaines, E. E., et al. (1997). The diffuse aurora: A significant source of ionization in the middle atmosphere. *Journal of Geophysical Research*, *102*(D23), 28,203–28,214. https://doi.org/10.1029/97JD02430

Fuller-Rowell, T. J., Codrescu, M. V., Moffett, R. J., & Quegan, S. (1994). Response of the thermosphere and ionosphere to geomagnetic storms. *Journal of Geophysical Research*, *99*(A3), 3893–3914. https://doi.org/10.1029/93JA02015

Fuller-Rowell, T. J., & Evans, D. S. (1987). Height-integrated Pedersen and Hall conductivity patterns inferred from the TIROS-NOAA satellite data. *Journal of Geophysical Research*, *92*, 7606–7618. https://doi.org/10.1029/JA092iA07p07606

Haaland, S. E., Paschmann, G., Förster, M., Quinn, J. M., Torbert, R. B., McIlwain, C. E., et al. (2007). High-latitude plasma convection from Cluster EDI measurements: Method and IMF-dependence. *Annales de Geophysique*, *25*, 239–253.

Hairston, M. R., & Heelis, R. A. (1990). Model of the high-latitude ionospheric convection pattern during southward interplanetary magnetic field using DE 2 data. *Journal of Geophysical Research*, *95*(A3), 2333–2343. https://doi.org/10.1029/JA095iA03p02333

Hardy, D. A., Gussenhoven, M. S., Raistrick, R., & McNeil, W. J. (1987). Statistical and functional representations of the pattern of auroral energy flux, number flux, and conductivity. *Journal of Geophysical Research*, *92*(A11), 12,275–12,294. https://doi.org/10.1029/JA092iA11p12275

Hardy, D. A., Holeman, E. G., Burke, W. J., Gentile, L. C., & Bounar, K. H. (2008). Probability distributions of electron precipitation at high magnetic latitudes. *Journal of Geophysical Research*, *113*.

Heppner, J. P., & Maynard, N. C. (1987). Empirical high-latitude electric field models. *Journal of Geophysical Research*, *92*(A5), 4467–4489. https://doi.org/10.1029/JA092iA05p04467

Holt, J. M., Wand, R. H., Evans, J. V., & Oliver, W. L. (1987). Empirical models for the plasma convection at high latitudes from Millstone Hill observations. *Journal of Geophysical Research*, *92*(A1), 203–212. https://doi.org/10.1029/JA092iA01p00203

Holzworth, R. H., & Meng, C. (1975). Mathematical representation of the auroral oval. *Geophysical Research Letters*, *2*, 377–380. https://doi.org/10.1029/GL002i009p00377

Kilcommons, L. M., Redmon, R. J., & Knipp, D. J. (2017). A new DMSP magnetometer and auroral boundary data set and estimates of field-aligned currents in dynamic auroral boundary coordinates. *Journal of Geophysical Research: Space Physics*, *122*, 9068–9079. https://doi.org/10.1002/2016JA023342

Liam Kilcommons, & Angeline Burrell. (2019, July 3). lkilcommons/ssj_auroral_boundary: Version 1 (Version v1.0.0). Zenodo. http://doi.org/10.5281/zenodo.3267415

Killeen, T. L., & Roble, R. G. (1984). An analysis of the high-latitude thermospheric wind pattern calculated by a thermospheric general circulation model: 1. Momentum forcing. *Journal of Geophysical Research*, *89*(A9), 7509–7522. https://doi.org/10.1029/JA089iA09p07509

Koustov, A. V., & Fiori, R. A. D. (2016). Seasonal and solar cycle variations in the ionospheric convection reversal boundary location inferred from monthly SuperDARN data sets. *Annales Geophysicae*, *34*, 227–239. https://doi.org/10.5194/angeo-34-227-2016

Lin, C. Y., Deng, Y., Sheng, C., & Drob, D. P. (2017). A study of the nonlinear response of the upper atmosphere to episodic and stochastic acoustic-gravity wave forcing. *Journal of Geophysical Research: Space Physics*, *122*, 1178–1198. https://doi.org/10.1002/2016JA022930

Liou, K., Meng, C.-I., & Wu, C.-C. (2006). On the interplanetary magnetic field B_y control of substorm bulge expansion. *Journal of Geophysical Research*, *111*, A09312. https://doi.org/10.1029/2005JA011556

Liou, K., Newell, P. T., & Meng, C.-I. (2001). Seasonal effects on auroral particle acceleration and precipitation. *Journal of Geophysical Research*, *106*(A4), 5531–5542. https://doi.org/10.1029/1999JA000391

Lu, G., Richmond, A. D., Emery, B. A., & Roble, R. G. (1995). Magnetosphere-ionosphere-thermosphere coupling: Effect of neutral winds on energy transfer and field-aligned current. *Journal of Geophysical Research*, *100*, 19,643–19,660. https://doi.org/10.1029/95JA00766

Lu, G., Richmond, A. D., Lühr, H., & Paxton, L. (2016). High-latitude energy input and its impact on the thermosphere. *Journal of Geophysical Research: Space Physics*, *121*, 7108–7124. https://doi.org/10.1002/2015JA022294

Luan, X., Zhou, S., & Dou, X. (2018). Auroral energy flux distribution over the nightside auroral oval observed by the DMSP F16/SSUSI: Seasonal, geomagnetic, and solar activity dependences. *Journal of Geophysical Research: Space Physics*, *123*, 4457–4466. https://doi.org/10.1029/2017JA023970

Mitchell, E. J., Newell, P. T., Gjerloev, J. W., & Liou, K. (2013). OVATION-SM: A model of auroral precipitation based on SuperMAG generalized auroral electrojet and substorm onset times. *Journal of Geophysical Research: Space Physics*, *118*, 3747–3759. https://doi.org/10.1002/jgra.50343

Newell, P. T., Burke, W. J., Sánchez, E. R., Meng, C. I., Greenspan, M. E., & Clauer, C. R. (1991). The lowlatitude boundary layer and the boundary plasma sheet at low altitude: Prenoon precipitation regions and convection reversal boundaries. *Journal of Geophysical Research*, *96*(A12), 21,013–21,023.

Newell, P. T., Feldstein, Y. I., Galperin, Y. I., & Meng, C.-I. (1996). Morphology of nightside precipitation. *Journal of Geophysical Research*, *101*(A5), 10,737–10,748. https://doi.org/10.1029/95JA03516

Newell, P. T., Ruohoniemi, J. M., & Meng, C.-I. (2004). Maps of precipitation by source region, binned by IMF, with inertial convection streamlines. *Journal of Geophysical Research*, *109*, A10206. https://doi.org/10.1029/2004JA010499

Newell, P. T., Sotirelis, T., & Wing, S. (2009). Diffuse, monoenergetic, and broadband aurora: The global precipitation budget. *Journal of Geophysical Research*, *114*, A09207. https://doi.org/10.1029/2009JA014326

Papitashvili, V. O., & Rich, F. J. (2002). High-latitude ionospheric convection models derived from Defense Meteorological Satellite Program ion drift observations and parameterized by the interplanetary magnetic field strength and direction. *Journal of Geophysical Research*, *107*(A8), 1198. https://doi.org/10.1029/2001JA000264

Pedatella, N. M., Lu, G., & Richmond, A. D. (2018). Effects of high-latitude forcing uncertainty on the low-latitude and midlatitude ionosphere. *Journal of Geophysical Research: Space Physics*, *123*, 862–882. https://doi.org/10.1002/2017JA024683

Prölss, G. W. (1995). Ionospheric *F*-region storms. In H. Volland (Ed.), *Handbook of Atmospheric Electrodynamics* (pp. 195–248). Boca Raton, FL: CRC Press.

Redmon, R. J., Denig, W. F., Kilcommons, L. M., & Knipp, D. J. (2017). New DMSP database of precipitating auroral electrons and ions. *Journal of Geophysical Research: Space Physics*, *122*, 9056–9067. https://doi.org/10.1002/2016JA023339

Redmon, R. J., Peterson, W. K., Andersson, L., Kihn, E. A., Denig, W. F., Hairston, M., & Coley, R. (2010). Vertical thermal O^+ flows at 850 km in dynamic auroral boundary coordinates. *Journal of Geophysical Research*, *115*, A00J08. https://doi.org/10.1029/2010JA015589

Rees, M. H. (1989). *Physics and chemistry of the upper atmosphere* (Vol. 1). Cambridge: Cambridge University Press.

Reiff, P. H., & Burch, J. L. (1985). IMF By-dependent plasma flow and Birkeland currents in the dayside magnetosphere: 2. A global model for northward and southward IMF. *Journal of Geophysical Research*, *90*(A2), 1595–1609. https://doi.org/10.1029/JA090iA02p01595

Rich, F. J., & Hairston, M. (1994). Large-scale convection patterns observed by DMSP. *Journal of Geophysical Research*, *99*(A3), 3827–3844. https://doi.org/10.1029/93JA03296

Richmond, A. D., & Kamide, Y. (1988). Mapping electrodynamic features of the high-latitude ionosphere from localized observations: Technique. *Journal of Geophysical Research*, *93*(A6), 5741–5759. https://doi.org/10.1029/JA093iA06p05741

Ridley, A. J., Deng, Y., & Tóth, G. (2006). The global ionosphere thermosphere model. *Journal of Atmospheric and Solar-Terrestrial Physics*, *68*, 839–864. https://doi.org/10.1016/j.jastp.2006.01.008

Ruohoniemi, J. M., & Greenwald, R. A. (1996). Statistical patterns of high-latitude convection obtained from Goose Bay HF radar observations. *Journal of Geophysical Research*, *101*(A10), 21,743–21,763. https://doi.org/10.1029/96JA01584

Ruohoniemi, J. M., & Greenwald, R. A. (2005). Dependencies of high-latitude plasma convection: Consideration of interplanetary magnetic field, seasonal, and universal time factors in statistical patterns. *Journal of Geophysical Research*, *110*, A09204. https://doi.org/10.1029/2004JA010815

Sotirelis, T., & Newell, P. T. (2000). Boundary-oriented electron precipitation model. *Journal of Geophysical Research*, *105*(A8), 18,655–18,673. https://doi.org/10.1029/1999JA000269

Sotirelis, T., Ruohoniemi, J. M., Barnes, R. J., Newell, P. T., Greenwald, R. A., Skura, J. P., & Meng, C.-I. (2005). Comparison of SuperDARN radar boundaries with DMSP particle precipitation boundaries. *Journal of Geophysical Research*, *110*, A06302. https://doi.org/10.1029/2004JA010732

Thayer, J. P., Vickrey, J. F., Heelis, R. A., & Gary, J. B. (1995). Interpretation and modeling of the high-latitude electromagnetic energy flux. *Journal of Geophysical Research*, *100*, 19,715–19,728. https://doi.org/10.1029/95JA01159

Thébault, E., Finlay, C. C., Beggan, C. D., Alken, P., Aubert, J., Barrois, O., et al. (2015). International geomagnetic reference field: The 12th generation. *Earth, Planets and Space*, *67*(1), 1–19.

Thomas, E. G., & Shepherd, S. G. (2018). Statistical patterns of ionospheric convection derived from mid-latitude, high-latitude, and polar SuperDARN HF radar observations. *Journal of Geophysical Research: Space Physics*, *123*, 3196–3216. https://doi.org/10.1002/2018JA025280

Torr, D. G., Torr, M. R., Brinton, H. C., Brace, L. H., Spencer, N. W., Hedin, A. E., et al. (1979). An experimental and theoretical study of the mean diurnal variation of O^+, NO^+, O_2^+, and N_2^+ ions in the mid-latitude F_1 layer of the ionosphere. *Journal of Geophysical Research*, *84*(A7), 3360–3372. https://doi.org/10.1029/JA084iA07p03360

Wallis, D., & Budzinski, E. E. (1981). Empirical models of height integrated conductivities. *Journal of Geophysical Research*, *86*(A1), 125–137. https://doi.org/10.1029/JA086iA01p00125

Weimer, D. R. (2005). Improved ionospheric electrodynamic models and application to calculating Joule heating rates. *Journal of Geophysical Research*, *110*, A05306. https://doi.org/10.1029/2004JA010884

Zhang, S.-R., Holt, J. M., & McCready, M. (2007). High latitude convection based on long-term incoherent scatter radar observations in North America. *Journal of Atmospheric and Solar-Terrestrial Physics*, *69*, 1273–1291. https://doi.org/10.1016/j.jastp.2006.08.017

Zhang, Y., & Paxton, L. J. (2008). An empirical Kp-dependent global auroral model based on TIMED/GUVI FUV data. *Journal of Atmospheric and Solar-Terrestrial Physics*, *70*, 1231–1242. https://doi.org/10.1016/j.jastp.2008.03.008

Zhu, Q., Deng, Y., Maute, A., Sheng, C., & Lin, C. Y. (2017). Impact of the vertical dynamics on the thermosphere at low and middle latitudes: GITM simulations. *Journal of Geophysical Research: Space Physics*, *122*, 6882–6891. https://doi.org/10.1002/2017JA023939